

STELLAR WINDS, DEAD ZONES, AND CORONAL MASS EJECTIONS

R. KEPPENS AND J. P. GOEDBLOED

FOM—Institute for Plasma-Physics Rijnhuizen, P.O. Box 1207, 3430 BE Nieuwegein, Netherlands; keppens@rijnh.nl

Received 1999 May 10; accepted 1999 October 6

ABSTRACT

Axisymmetric stellar wind solutions are presented that were obtained by numerically solving the ideal magnetohydrodynamic (MHD) equations. Stationary solutions are critically analyzed using the knowledge of the flux functions. These flux functions enter in the general variational principle governing all axisymmetric stationary ideal MHD equilibria. The magnetized wind solutions for (differentially) rotating stars contain both a “wind” and a “dead” zone. We illustrate the influence of the magnetic field topology on the wind acceleration pattern by varying the coronal field strength and the extent of the dead zone. This is evident from the resulting variations in the location and appearance of the critical curves for which the wind speed equals the slow, Alfvén, and fast speed. Larger dead zones cause effective, fairly isotropic acceleration to super-Alfvénic velocities as the polar, open field lines are forced to fan out rapidly with radial distance. A higher field strength moves the Alfvén transition outward. In the ecliptic, the wind outflow is clearly modulated by the extent of the dead zone. The combined effect of a fast stellar rotation and an equatorial dead zone in a bipolar field configuration can lead to efficient thermocentrifugal equatorial winds. Such winds show both a strong poleward collimation and some equatorward streamline bending due to significant toroidal field pressure at midlatitudes. We discuss how coronal mass ejections are then simulated on top of the transonic outflows.

Subject headings: MHD — methods: numerical — solar wind — stars: winds, outflows

1. INTRODUCTION

The solar wind outflow presents a major challenge to numerical modeling since it is a fully three-dimensional, time-dependent physical environment, in which regions of supersonic and subsonic speeds coexist in a tenuous, magnetized plasma. *Ulysses* observations (McComas et al. 1998) highlighted again that the solar wind about the ecliptic plane is fundamentally dynamic in nature, while the fast speed wind across both solar poles is on the whole stationary and uniform. Recent *SOHO* measurements (Hassler et al. 1999) demonstrated how the fast wind emanating from coronal holes is rooted to the “honeycomb” structure of the chromospheric magnetic network, making the outflow truly three dimensional, while the daily coronal mass ejections (CMEs) are in essence highly time-varying. Moreover, one really needs to study these time-dependent, multi-dimensional aspects in conjunction with the coronal heating puzzle (Holzer & Leer 1997).

Working toward that goal, Wang et al. (1998) recently modeled the solar wind using a two-dimensional, time-dependent, magnetohydrodynamic (MHD) description with heat and momentum addition as well as thermal conduction. Their magnetic topology shows both open (polar) and closed (equatorial) field-line regions. When heating the closed field region, a sharp streamer-like cusp forms at its tip as the region continuously expands and evaporates. A quasi-stationary wind model results for which the emphasis is on reaching a qualitative and quantitative agreement with the observed latitudinal variation (reproducing, in particular, the sharp transition at roughly $\pm 20^\circ$ latitude between fast and slow solar wind) by tuning the spatial dependence of the artificial volumetric heating and momentum sources.

We follow another route toward global solar wind modeling, working our way up stepwise from stationary one-dimensional to three-dimensional (1D to 3D) MHD configurations. In a pure ideal, stationary, axisymmetric

MHD approach, numerical simulations can benefit greatly from analytical theory. This is demonstrated in Ustyugova et al. (1999), in which stationary magnetocentrifugally driven winds from rotating accretion disks were calculated numerically and critically verified by MHD theory.

In this paper, we extend the Wang et al. (1998) modeling efforts to 2.5 dimensions by including toroidal vector components while remaining axisymmetric. This allows us to explore stellar wind regimes in which rotation is also important. The magnetic field still has open and closed field-line regions, but in ideal MHD, the closed field region is a “dead” zone from which no plasma can escape. The unknown coronal heating is avoided by assuming a polytropic equation of state and dropping the energy equation all together. The stationary, axisymmetric, polytropic MHD models are analyzed as in Ustyugova et al. (1999).

In particular, we investigate the effects of (1) having both open and closed field-line regions in axisymmetric stellar winds and (2) time-dependent perturbations within these transonic outflows. While we still ignore the basic question of why there should be a hot corona in the first place, we make significant progress toward fully 3D, dynamic models. The advantages of a gradual approach toward such a “final” model were pointed out in Keppens & Goedbloed (1999a). There, we initiated our effort to numerically model stellar outflows by gradually relaxing the assumptions inherent in the most well-known solar wind model: the isothermal Parker wind (Parker 1958). In a sequence of stationary, 1D, 1.5D, and 2.5D, hydrodynamic and magnetohydrodynamic stellar wind models, all obtained with the Versatile Advection Code¹ (VAC; see Tóth 1996, 1997; Tóth & Keppens 1998; Keppens & Tóth 1999a), we demonstrated that we can now routinely calculate axisymmetric magnetized wind solutions for (differentially) rotating stars. An important generalization of previous modeling

¹ Information on VAC can be found at <http://www.phys.uu.nl/~toth>.

efforts (Sakurai 1985, 1990) is that the field topology can have both open and closed field-line regions, so we model wind and dead zones self-consistently. In essence, our work extends the early model efforts by Pneuman & Kopp (1971) in (1) going from an isothermal to a polytropic equation of state, (2) allowing for stellar rotation, and (3) including time-dependent phenomena. While we get qualitatively similar solutions for solar-like conditions, we differ entirely in the numerical procedure employed and in the way boundary conditions are specified. Keppens & Goedbloed (1999a) contained one such MHD model for fairly solar-like parameter values. In this paper, we start with a critical examination of this reference model. The obtained transonic outflow, accelerating from subslow to superfast speeds, must obey the conservation laws predicted by theory by conserving various physical quantities along streamlines. This will be checked in § 2. Section 3 continues with a physical analysis of the model and investigates the influence of the magnetic field strength and of the latitudinal extent of the dead zone. These parameters have a clear influence on the global wind structure, especially evident in the appearance and location of its critical surfaces where the wind speed equals the slow, Alfvén, and fast magnetosonic speeds. We also present one such wind solution for a star which rotates 20 times faster than our Sun. Finally, § 4 relaxes the stationarity of the wind pattern by forcing coronal mass ejections on top of the wind pattern. Conclusions are given in § 5.

2. REFERENCE MODEL AND CONSERVATION LAWS

2.1. Solution Procedure

We recall from Keppens & Goedbloed (1999a) that we solve the following conservation laws for the density ρ , the momentum vector $\rho\mathbf{v}$, and the magnetic field \mathbf{B} :

$$\frac{\partial \rho}{\partial t} + \nabla \cdot (\rho\mathbf{v}) = 0, \quad (1)$$

$$\frac{\partial(\rho\mathbf{v})}{\partial t} + \nabla \cdot [\rho\mathbf{v}\mathbf{v} + p_{\text{tot}}\mathbf{I} - \mathbf{B}\mathbf{B}] = \rho\mathbf{g}, \quad (2)$$

$$\frac{\partial \mathbf{B}}{\partial t} + \nabla \cdot (\mathbf{v}\mathbf{B} - \mathbf{B}\mathbf{v}) = 0. \quad (3)$$

Here, $p_{\text{tot}} = p + (1/2)B^2$ is the total pressure, \mathbf{I} is the identity tensor, and $\mathbf{g} = -(GM_*/r^2)\hat{\mathbf{e}}_r$ is the external stellar (mass M_*) gravitational field with r indicating radial distance. We assume $p \sim \rho^\gamma$ (dimensionless, we take $p = \rho^\gamma/\gamma$), where in this paper we only construct models for specified polytropic index $\gamma = 1.13$. This compares to the value 1.05 used in recent work by Wu, Guo, & Dryer (1997) and an empirically determined value of 1.46 derived from *Helios 1* data by Totten, Freeman, & Arya (1995).

The discretized equations (1)–(3) are solved on a radially stretched polar grid in the poloidal plane using a total variation diminishing Lax-Friedrich discretization (see, e.g., Tóth & Odstrčil 1996) with Woodward limiting (Collela & Woodward 1984). Stationary ($\partial/\partial t = 0$) solutions are identified when the relative change in the conservative variables from subsequent time steps drops below a chosen tolerance (sometimes down to 10^{-7}). We explained in Keppens & Goedbloed (1999a) how we benefited greatly from implicit time integration (see Tóth, Keppens, & Botchev 1998;

Keppens et al. 1999a; van der Ploeg, Keppens, & Tóth 1997) for obtaining axisymmetric ($\partial/\partial\phi = 0$) hydrodynamic ($\mathbf{B} = 0$) stellar outflows characterized by $\rho(R, Z)$ and $\mathbf{v}(R, Z)$, where (R, Z) are Cartesian coordinates in the poloidal plane. Denoting the base radius by r_* , these hydrodynamic models cover $r \in [1, 50]r_*$ and have as escape speed $v_{\text{esc}} = (2GM_*/r_*)^{1/2} = 3.3015c_{s*}$, with c_{s*} the base sound speed. They are also characterized by a rotational parameter $\zeta = \Omega_* r_*/c_{s*} = 0.0156$ (if not specified otherwise) and impose boundary conditions at the base such that (1) $v_\phi = \zeta R$ and (2) the poloidal base speed v_p is in accordance with a prescribed radial mass flux $\rho v_p = f_{\text{mass}} \hat{\mathbf{e}}_r/r^2$. The value of the mass-loss rate parameter f_{mass} is taken from a 1D polytropic, rotating Parker wind valid for the equatorial regions under identical parameter values. For $\zeta = 0.0156$, we get $f_{\text{mass}} = 0.01377$. We clarify below the way in which the values for the dimensionless quantities v_{esc}/c_{s*} , ζ , and f_{mass} relate to the prevailing solar conditions.

To arrive at a “reference” MHD wind solution, two more parameters enter the description that quantify the initial field strength and the desired extent of the dead zone. A stationary, axisymmetric, magnetized stellar wind is the end result of a time-stepping process which has the initial density $\rho(R, Z)$ and toroidal velocity component $v_\phi(R, Z)$ from the hydrodynamic (HD) solution with identical γ , v_{esc} , and ζ parameters. The poloidal velocity is also copied from the HD solution in a polar wind zone in which $\theta < \theta_{\text{wind}}$ (upper quadrant with $\theta = 0$ at pole), quantified by its polar angle θ_{wind} . The dead zone is appropriately initialized by a zero poloidal velocity. The field is initially set to a monopole field in the wind zone, where

$$\begin{aligned} B_R(R, Z; t = 0) &= B_0 R/r^3, \\ B_Z(R, Z; t = 0) &= B_0 Z/r^3, \end{aligned} \quad (4)$$

where $r^2 = R^2 + Z^2$, coupled to a dipole field in the dead zone with

$$\begin{aligned} B_R(R, Z; t = 0) &= 3a_d \frac{ZR}{r^5}, \\ B_Z(R, Z; t = 0) &= a_d \frac{(2Z^2 - R^2)}{r^5}. \end{aligned} \quad (5)$$

The strength of the dipole is taken to be $a_d = B_0/(2 \cos \theta_{\text{wind}})$ to keep the radial field component B_r continuous at $\theta = \theta_{\text{wind}}$. The initial B_ϕ component is zero throughout. Keppens & Goedbloed (1999a) took $B_0 = 3.69$ and $\theta_{\text{wind}} = 60^\circ$, so that the corresponding dead zone covered only a $\pm 30^\circ$ latitudinal band about the stellar equator. For the Sun at minimum activity, the extent of the coronal hole is typically such that $\theta_{\text{wind}} = 30^\circ$, so it will be useful to vary this parameter in what follows (§ 3). We use a resolution of 300×40 in the full poloidal half-plane, impose symmetry conditions at both poles, and we use a free outflow at the outer radius $50r_*$ (where all quantities are extrapolated linearly in ghost cells). At the stellar base, we similarly extrapolate density and all magnetic field components from their initial values, but let these quantities adjust in value while keeping this initial gradient in the ghost cells. This implies that the density and the magnetic field at the base is determined during the time-stepping process to arrive at steady state. We enforce the $\nabla \cdot \mathbf{B} = 0$ condition using a projection scheme (Brackbill & Barnes 1980) to end up with a physically realistic magnetic configura-

ration (despite the “monopolar” field in the wind zone). The stellar boundary condition for the momentum equation allows us to specify a differential rotation rate $\zeta(\theta)$ and latitudinally varying mass flux through $f_{\text{mass}}(\theta)$. We set

$$\rho v_p = f_{\text{mass}}(\theta) \hat{e}_r / r^2, \quad v_\phi = \zeta(\theta) R + B_\phi v_p / B_p. \quad (6)$$

The reference model has a rigid rotation rate according to $\zeta = 0.0156$, while $f_{\text{mass}} = 0.01377$ in the wind region and zero in the equatorial dead zone.

As emphasized in Keppens & Goedbloed (1999a), our choice of boundary conditions is motivated by the variational principle governing all axisymmetric, stationary, ideal MHD equilibria (see § 2.2). The analytic treatment shows that the algebraic Bernoulli equation, together with the cross-field momentum balance, really determines the density profile and the magnetic flux function concurrently. In keeping with this formalism, we impose a base mass flux and a stellar rotation and let the density and the magnetic field configuration adjust freely at the base. In prescribing the stellar rotation, we exploit the freedom available in the variational principle by setting a flux function at the base. It is noteworthy that the Pneuman & Kopp (1971) model, as well as many more recent modeling efforts for stellar MHD winds, fixes the base normal component of the magnetic field together with the density. Below, we demonstrate that our calculated meridional density structure compares well with recent observations by Gallagher et al. (1999).

The values for the dimensionless parameters $v_{\text{esc}}/c_{\text{ss}}$, ζ , and B_0 (actually the ratio of the coronal Alfvén speed to c_{ss}) are solar-like in the following sense. At a reference radius $r_* = 1.25 R_\odot$, we take values for the number density $N_0 \simeq 10^8 \text{ cm}^{-3}$, temperature $T_0 = 1.5 \times 10^6 \text{ K}$, coronal field strength $B_0 \simeq 2 \text{ G}$, and rotation rate $\Omega_\odot = 2.998 \times 10^{-6} \text{ s}^{-1}$. For $\gamma = 1.13$ and assuming a mean molecular weight $\tilde{\mu} = 0.5$, the base sound speed then turns out to be $c_{\text{ss}} = 167.241 \text{ km s}^{-1}$, with all dimensionless ratios as used in the reference model. Further, the value for the mass-loss rate parameter $f_{\text{mass}} = 0.01377$ is then in units of $1.06 \times 10^{13} \text{ g s}^{-1}$, so that a split-monopole magnetic configuration leads to a realistic mass-loss rate $\dot{M} \propto 4\pi f_{\text{mass}} \simeq 2.9 \times 10^{-14} M_\odot \text{ yr}^{-1}$. Since the reference model has a constant mass flux in its wind zone, the presence of the dead zone reduces this value by exactly $(1 - \cos \theta_{\text{wind}}) = \frac{1}{2}$. Units enter through the reference radius r_* , the base sound speed c_{ss} , and the base density $\rho_* = N_0 m_p \tilde{\mu}$ (with proton mass m_p).

2.2. Stream Functions

The final stationary wind pattern is shown below in Figure 3 (see also Fig. 5 in Keppens & Goedbloed 1999a). The physical correctness of this numerically obtained ideal MHD solution can be checked as follows. All axisymmetric stationary ideal MHD equilibria are derivable from a single variational principle $\delta L = \delta \int \mathcal{L} dV = 0$ with Lagrangian density (Goedbloed, Keppens, & Lifschitz 1998; Keppens & Goedbloed 1999b):

$$\mathcal{L}(M^2, \psi, \nabla\psi; R, Z) = \frac{1}{2R^2} (1 - M^2) |\nabla\psi|^2 - \frac{\Pi_1}{M^2} + \frac{\Pi_2}{\gamma M^{2\gamma}} - \frac{\Pi_3}{1 - M^2}. \quad (7)$$

To obtain an analytic ideal MHD solution, the minimizing Euler-Lagrange equations need to be solved simultaneously for the poloidal flux function $\psi(R, Z)$ and the squared poloi-

dal Alfvén Mach number $M^2(R, Z) \equiv \rho v_p^2 / B_p^2$. Here, $B_p = (1/R) \hat{e}_\phi \times \nabla\psi$. In contrast with the translationally symmetric case (Goedbloed & Lifschitz 1997; Lifschitz & Goedbloed 1997), the governing variational principle contains factors R^2 , while the profiles Π_1 and Π_3 are no longer flux functions. In particular,

$$\Pi_1 \equiv \chi'^2 \left(H + \frac{R^2 \Omega^2}{2} + \frac{GM_*}{r} \right), \quad (8)$$

$$\Pi_2 \equiv \frac{\gamma}{\gamma - 1} \chi'^{2\gamma} S, \quad (9)$$

$$\Pi_3 \equiv \frac{\chi'^2}{2} \left(R\Omega - \frac{\Lambda}{R} \right)^2, \quad (10)$$

where five flux functions H , Ω , S , Λ , and χ' enter. These direct integrals of the axisymmetric, stationary ideal MHD equations are as follows:

1. The Bernoulli function (\sim energy):

$$H(\psi) \equiv \frac{1}{2} v^2 + \frac{\rho^{\gamma-1} \gamma S}{\gamma - 1} - \frac{GM_*}{r} - v_\phi^2 + v_\phi B_\phi \frac{v_p}{B_p}. \quad (11)$$

2. The derivative of the stream function $\chi' \equiv \partial\chi/\partial\psi$. Indeed, the poloidal stream function $\chi(R, Z)$ necessarily obeys $\chi(\psi)$, provided that the toroidal component of the electric field vanishes. These are immediate checks on the numerical solution, namely $v_R B_Z = v_Z B_R$, or the fact that streamlines and field lines in the poloidal plane must be parallel (easily seen in Fig. 3).

3. The entropy S , which for our *polytropic* numerical solutions is constant by construction: $S \equiv 1/\gamma$.

4. A quantity related to the angular momentum flux $F_{\text{AM}} = \rho v_p R v_\phi - B_p R B_\phi \equiv \rho v_p \Lambda$, defined as

$$\Lambda(\psi) \equiv R v_\phi - R B_\phi \frac{B_p}{\rho v_p}. \quad (12)$$

5. The derivative of the electric field potential

$$\Omega(\psi) \equiv \frac{1}{R} \left(v_\phi - \frac{v_p}{B_p} B_\phi \right). \quad (13)$$

Various combinations of these flux functions can be made; for instance, Goedbloed & Lifschitz (1997) used the following flux function (instead of Λ):

$$I(\psi) \equiv R B_\phi - R v_\phi \frac{\rho v_p}{B_p} = -\chi' \Lambda. \quad (14)$$

Figure 1 presents grayscale contour plots of three stream functions— I (actually $\log |I|$), Λ , and H —calculated from the reference solution, with its poloidal field lines overlaid. Ideally, these contours must match the field-line structure exactly: all deviations are due to numerical errors. Inspection shows that the agreement is quite satisfactory. A quantitative measure of the errors is given in the lower two frames. At bottom left, we plotted the relative deviation of Ω from the value enforced at the base $\zeta(\theta)$ (constant to 0.0156 in this model). The solid line marks the 10% deviation; actual values range from [0.0092, 0.0187]. It should be

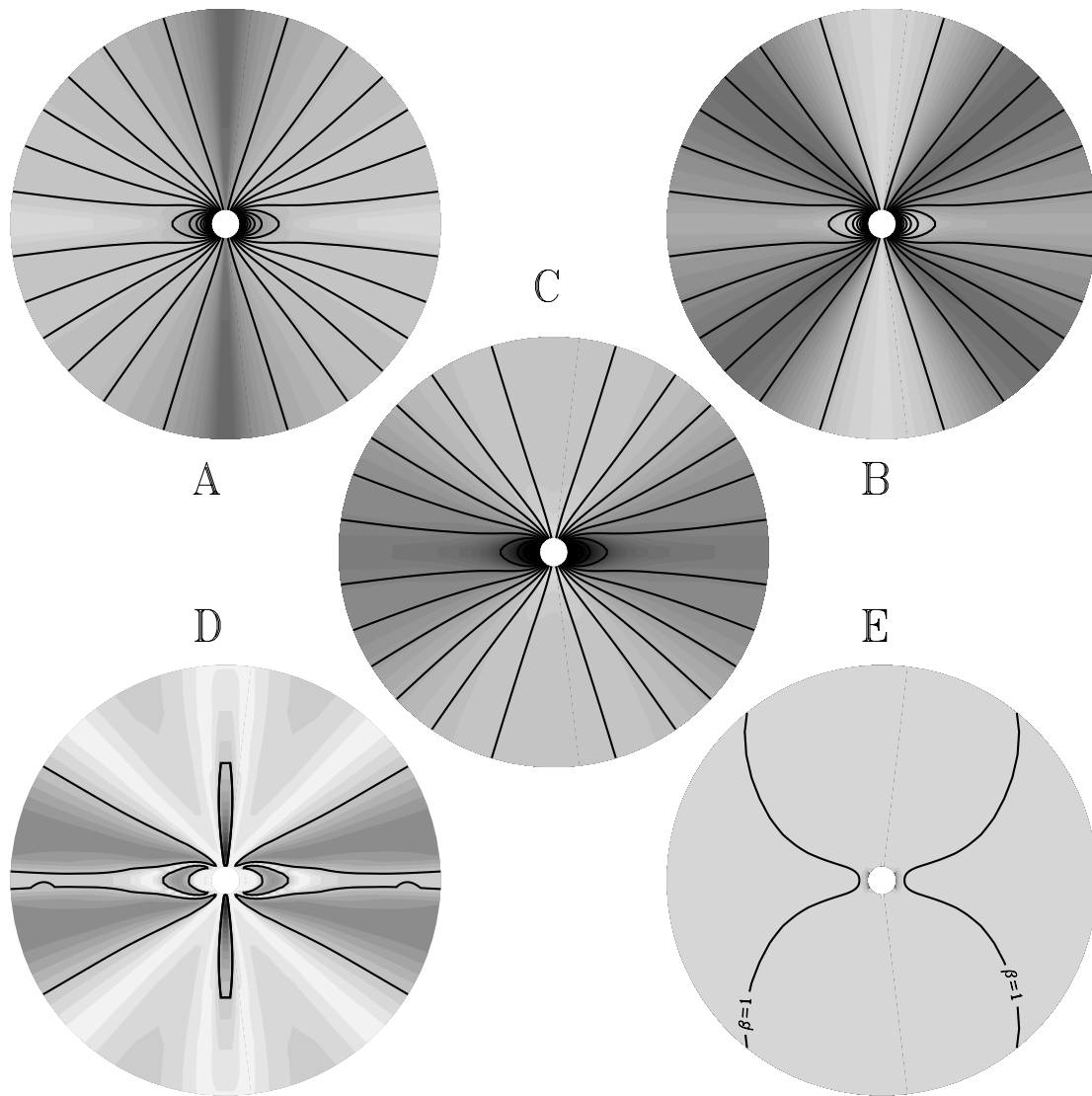


FIG. 1.—Numerical, ideal MHD stellar wind can be checked to conserve various quantities along poloidal streamlines and field lines. For the reference solution, the poloidal field lines (solid lines) must be isolevels in the contour plots of (A) the flux function I (plotted is $\log |I|$), (B) the flux function Λ , and (C) the Bernoulli function H . A quantitative error estimate is shown in panel (D) in which we plot $|\Omega - \zeta|/\zeta$, where the solid lines delineate dark-shaded regions with deviations $> 10\%$. Panel (E) shows in a contour plot of E_ϕ that this toroidal electric field component vanishes nearly everywhere. The solid line in (E) indicates the $\beta = 1$ isopleth.

noted that this is a very stringent test of the solution since for the chosen parameters, the wind is purely thermally driven, and the stellar rotation is dynamically unimportant. The largest deviations are apparent at the rotation axis (symmetry axis) in Ω , which is not unexpected due to its $1/R$ dependence. Other inconsistencies are in the region which has drastically changed from its initial zero velocity, purely dipole magnetic field structure: open field lines coming from the polar regions are now draped around a dipolar “dead” zone of limited radial extent. This dead zone simply corotates with the base angular velocity and has a vanishing poloidal velocity v_p and toroidal field B_ϕ . Around that zone, the stellar wind traces the open field lines. The final bottom right-hand frame shows E_ϕ , virtually vanishing everywhere, and only at the very base are values of order $\mathcal{O}(10^{-2})$. For completeness, we show the plasma beta $\beta = 2p/B^2 = 1$ contour which exceeds unity in an hourglass pattern that stretches out from the dead zone to large radial distances.

Overall, the obtained stationary numerical solution passes all criteria for being physically acceptable. We expect

that most errors disappear when using a higher resolution. We already exploited a radial grid accumulated near the stellar surface, necessary for resolving the near-surface acceleration. However, we could benefit also from a higher resolution in polar angle, now only 40 points for the full half-circle, by, for instance, using the up-down symmetry.

3. EXTENSIONS OF THE REFERENCE MODEL

With the accuracy of the numerical solutions confirmed by inspection of the stream functions, we can start the discussion of the influence of the physical parameters B_0 , θ_{wind} , and ζ on the global wind structure. First, we present a more detailed analysis of the reference solution itself.

Figure 2 shows the density structure in the left panel, where we plot number density as a function of polar angle for three fixed radial distances, namely at the base $1.27 R_\odot$, at $11.9 R_\odot$, and at $12.7 R_\odot$. Keppens & Goedbloed (1999a) already demonstrated the basic effect visible here: the equatorial density is higher than the polar density. A recent determination of the (r, θ) dependence of the coronal elec-

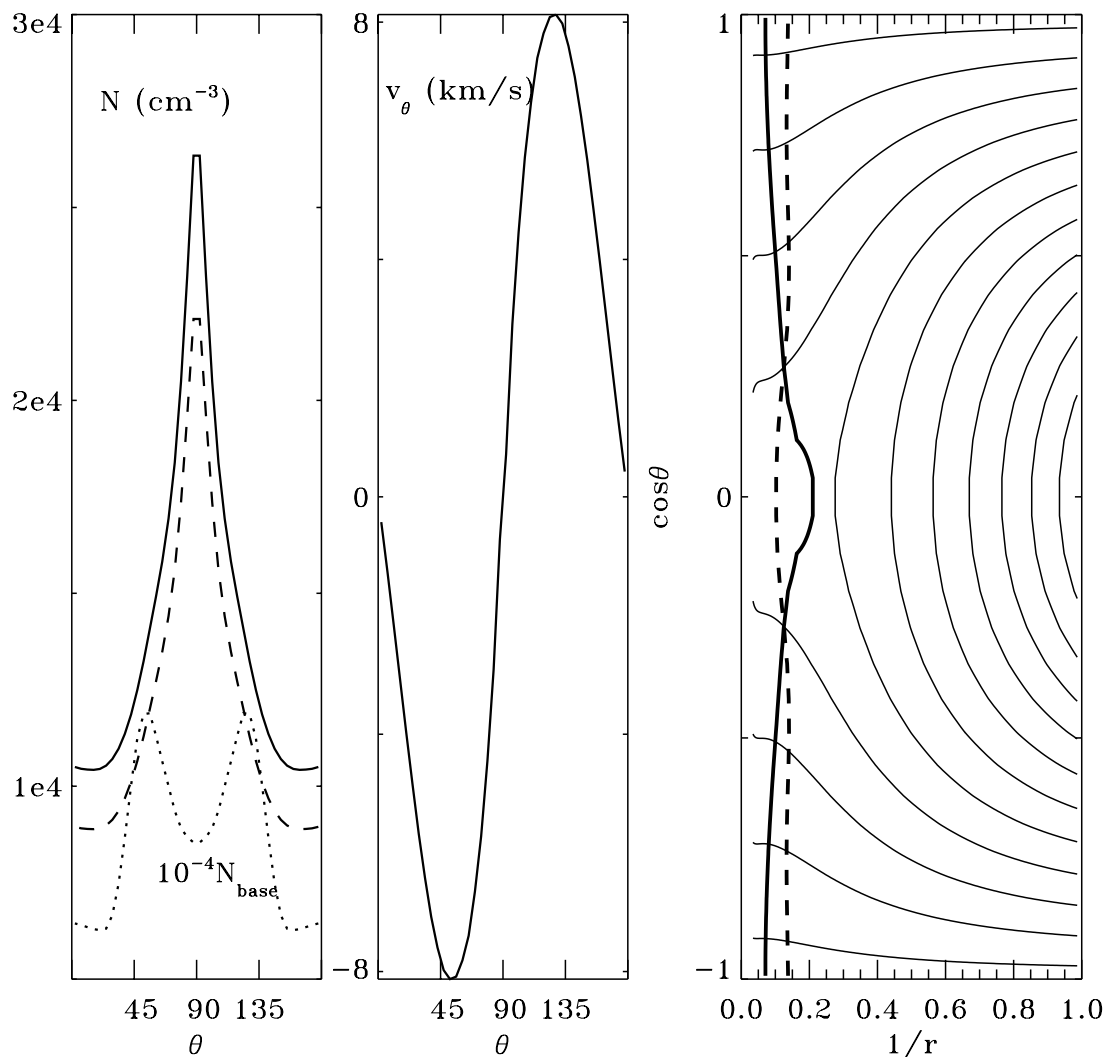


FIG. 2.—Analysis of the reference solar wind solution. *Left*: Number density from pole to pole at three fixed radial distances: $11.9 R_\odot$ (solid line), $12.7 R_\odot$ (dashed line), and at the base $1.27 R_\odot$ (dotted line, scaled to fit on the figure). *Middle*: Meridional velocity component v_θ as function of polar angle at a fixed $50 R_\odot$. *Right*: Magnetic field configuration and the poloidal sonic (dashed line) and poloidal Alfvén (solid line) surface as in Pneuman & Kopp (1971).

tron densities within $1 R_\odot \leq r \leq 1.2 R_\odot$ by Gallagher et al. (1999) concluded that the density falloff is faster in the equatorial region than at the poles and that the equatorial densities within the observed region are a factor of 3 larger than in the polar coronal hole. Their study lists number densities of order 10^8 cm^{-3} , as in our reference model. Our base density at $1.27 R_\odot$ (Fig. 2, left, dotted line) has a distinct latitude variation reflecting the combined open-closed field-line structure. Interestingly, the observations in Gallagher et al. (1999) show a similar structure, with quoted values of $8.3 \times 10^7 \text{ cm}^{-3}$ at $1.2 R_\odot$ above the pole, increasing to $1.6 \times 10^8 \text{ cm}^{-3}$ at the same distance along the equator. In fact, a dip in the density variation was present due to an active region situated above the equator. Qualitatively, we recover this variation at the boundary of the dead zone. Again, we stress that the base density is calculated self-consistently, hence, not imposed as a base boundary condition. The other two radial cuts situated beyond the dead zone agree quite well with the conclusions drawn by the observational study.

The reference wind solution also conforms with some well-known studies in MHD wind modeling. Suess &

Nerney (1973) and Nerney & Suess (1975) pointed out how consistent axisymmetric stellar wind modeling which includes magnetic fields and rotation automatically leads to a meridional flow away from the equator. At large radial distances, the flow profile should be of the form $v_\theta \propto -\sin(2\theta)$, with a poleward collimation of the magnetic field. This variation in polar angle is general and independent of the precise base field structure. In the middle panel of Figure 2, we show the latitude dependence of v_θ at $50 R_\odot$ for the reference model. Note the perfect agreement with the predicted variation.

Since the solar rotation rate, quantified by the parameter ζ , is low, the calculated wind solution in the poloidal plane should be similar to the one presented by Pneuman & Kopp (1971). They constructed purely poloidal, isothermal, and axisymmetric models of the solar wind including a helmet streamer (or “dead” zone). An iterative technique was used to solve for the steady coronal expansion, while the density and the radial magnetic field were fixed at the base. They enforced a dipolar B_r with a strength of 1 G at the poles, half the value we use at the initialization. Their uniform coronal temperature was taken to be $1.56 \times 10^6 \text{ K}$,

almost identical to our base temperature T_0 . Their base number density was imposed to be $1.847 \times 10^8 \text{ cm}^{-3}$, independent of latitude, and they assumed a slightly higher value for the mean molecular weight, namely $\tilde{\mu} = 0.608$. This leads to a base density which is a factor of 2.246 higher than the one used in our model. With these differences in mind (together with our polytropic equation of state and the rotational effects), we show in the right panel of Figure 2 the magnetic structure and the location of the sonic (where $v_p = c_s$) and the Alfvénic surface (where $v_p = B_p/\rho^{1/2}$) in a manner used in the original publication of Pneuman & Kopp (1971), their Figure 4. In the $(1/r, \cos \theta)$ projection, the Alfvénic transition on the equator is at the cusp of the helmet structure before the sonic point, while the sonic surface is closer to the solar surface at the poles. The qualitative agreement is immediately apparent, although our solution method is completely different, most notably in the prescription of the boundary conditions. By calculating the base density and magnetic field configuration self-consistently, we generalize the solution procedure employed by Pneuman & Kopp (1971) as we gain control of the size of the dead zone through our parameter θ_{wind} . This allows us to study the influence of the base topology of the magnetic field on the global wind acceleration pattern in what follows.

Figure 3 confronts three steady state wind solutions with our reference model, which differ in the latitudinal extent of the dead zone and/or in the magnetic field strength. With $\theta_{\text{wind}} = 60^\circ$ and $B_0 = 3.69$ (corresponding to a 2 G base coronal field strength) for the reference case A, we increased the latitudinal extent of the dead zone by taking $\theta_{\text{wind}} = 30^\circ$ in case B, doubled the field strength parameter B_0 in model C, and took both $B_0 = 7.4$ and $\theta_{\text{wind}} = 30^\circ$ to arrive at model D. We recall that B_0 specifies only the initial field strength used in the time-stepping process toward a stationary solution. The final base field strength turns out to be of roughly the same magnitude but differs in its detailed latitudinal variation. The changes in the global wind pattern are qualified by the resulting deformations of the critical surfaces (*hourglass curves*) where the wind speed equals the slow, Alfvén, and fast speeds. The plotted region stretches out to $\approx 18r_* \sim 22.5 R_\odot$.

By enlarging the dead zone under otherwise identical conditions (from A to B), the polar, open field lines are forced to fan out more rapidly with radial distance. As a result, the acceleration of the plasma occurs closer to the stellar surface, and the critical curves become somewhat more isotropic in polar angle. The Alfvén surface moves inward at the poles and shifts outward above the now larger dead zone at the equator, approaching a circle with an equatorial imprint of the dead zone. If we keep the dead zone small, but double the initial field strength B_0 (from A to C), the opposite behavior occurs: the critical curves, hence the entire acceleration behavior of the wind, become much more anisotropic. The most pronounced change is an inward shift of the polar slow transition and an outward shift of the Alfvén and fast polar transition. This behavior is in agreement with what a Weber-Davis model (Weber & Davis 1967) predicts to happen when the field strength is increased (note that the Weber-Davis model only applies to the equatorial region). When both the field strength and the dead zone are doubled (from A to D), the resulting Alfvén and fast critical curves are rather isotropic due to the influence of the dead zone. The polar slow transition is displaced

inward while the polar Alfvén and fast curve are shifted outward, as expected for the higher field. The detailed equatorial behavior is clearly modulated by the existing dead zone. We note that all wind solutions presented are still thermally driven, since the solar-like rotation rate is rather low and the field strengths are very modest. The changes are entirely due to reasonable variations in magnetic field topology and only a factor of 2 in field strength. One could tentatively argue that such variations occur in the solar wind pattern within its 11 yr magnetic cycle. In grayscale, Figure 3 shows the absolute value of the toroidal field component $|B_\phi|$ (this field changes sign across the equator). Note that the stellar rotation has wound up the field lines in a zone midway between the poles and the dead zone. For higher rotation rates (see below), the associated magnetic pressure buildup due to rotation can influence the wind pattern and cause collimation (Trussoni, Tsinganos, & Sauty 1997). Due to the four-lobe structure, one can expect parameter regimes which lead to both poleward collimation (as in the monopole-field models of Sakurai 1985) and equatorward streamline bending.

Figure 4 compares the radial dependence of the poloidal velocity for the four models (A, B, C, D) at the pole (*left panel*) and the equator (*middle panel*). For comparison, we overplotted the same quantities in each panel for a solution with a split-monopole base field at the same parameter values. This monopolar field solution is identical in nature to the Sakurai (1985, 1990) models and was shown in Keppens & Goedbloed (1999a; their Fig. 4). At the pole, a faster acceleration to higher speeds as compared to the reference model results from either increasing the field strength or enlarging the dead zone. Moreover, all four models show a faster initial acceleration than the corresponding monopolar field model. Radio-scattering measurements of the polar solar wind speed (Grall et al. 1996) indicated that the polar wind acceleration is almost complete by $10 R_\odot$, much closer than expected. Our model calculations show that a fast acceleration can result from modest increases in the coronal field strength and dead zone extent (model D has a solar-like dead zone of $\pm 60^\circ$).

The middle panel of Figure 4 shows the distinct decrease in equatorial wind speed due to the dead zone, when compared to a split-monopole solution. The equatorial velocities are reduced by 10–40 km s^{-1} , depending on the size of the dead zone and the base field strength. Enlarging the dead zone reduces the wind speed significantly (compare A to B and C to D). To a lesser degree, the same effect is true for an increase in coronal field strength (compare A to C and B to D). Keppens & Goedbloed (1999a; their Fig. 6) contained a polar plot of the velocity and the density at a fixed radial distance for the reference model, in which at least qualitatively a transition from high-density, low-speed equatorial wind to lower density, high-speed polar wind is noticeable. As evidenced by Figure 4, this difference in equatorial and polar wind is even more pronounced for larger dead zones. The velocities reached are too low for explaining the solar wind speeds—the Weber-Davis wind solution of identical parameters reaches 263 km s^{-1} at 1 AU. However, this is a well-known shortcoming of a polytropic MHD description for modeling the solar wind. Wu et al. (1999) therefore resort to an ad hoc procedure in which the polytropic index is an increasing function of radial distance $\gamma(r)$ to attain a more realistic 420 km s^{-1} wind speed at 1 AU, corresponding to the “slow” solar wind. A more

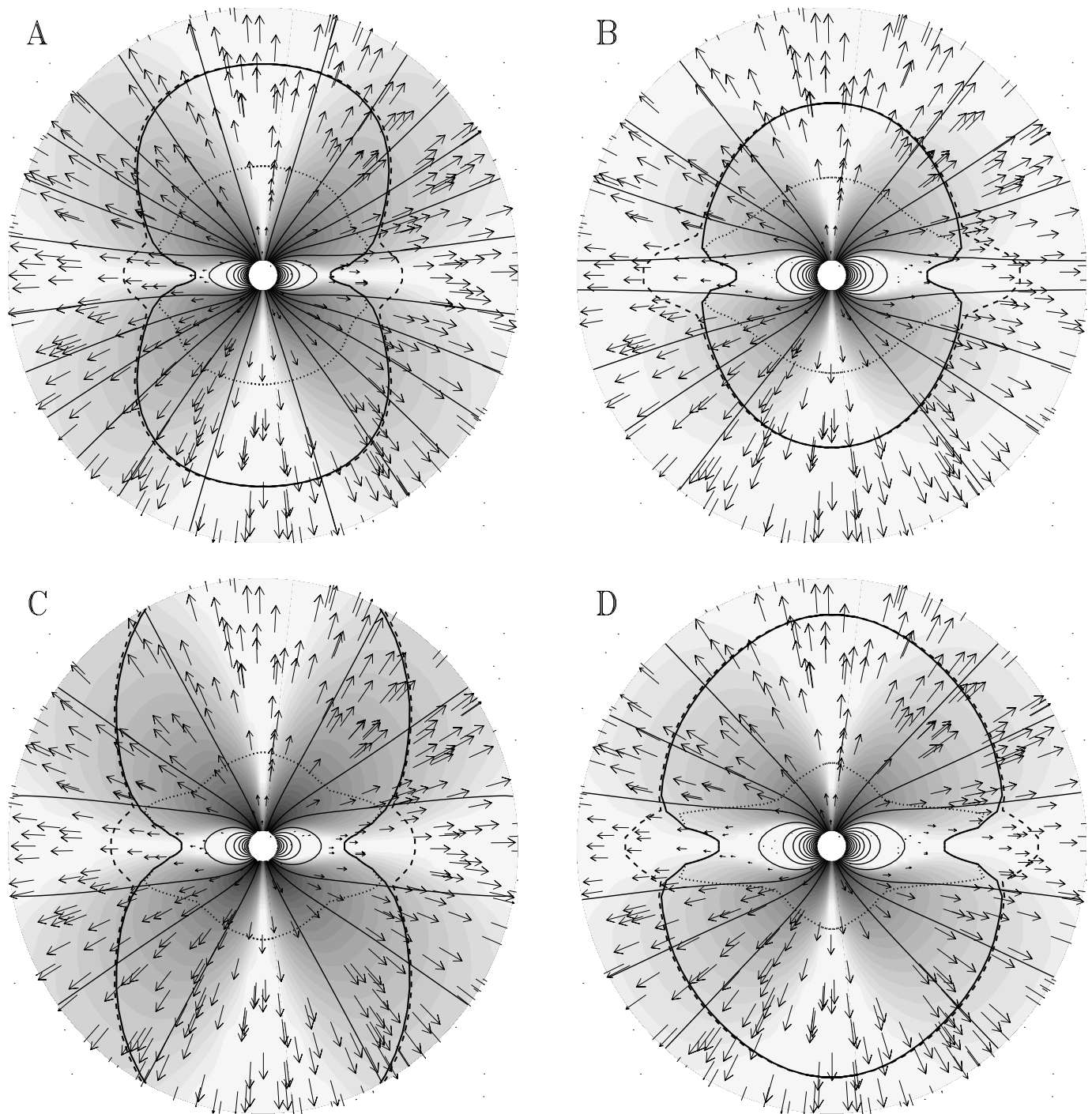


FIG. 3.—Variation in the detailed wind acceleration pattern due to changes in the stellar magnetic field. Poloidal cuts with the star at the center contain magnetic field lines (*solid lines*) and poloidal flow vectors, necessarily parallel to the field lines. The hourglass curves indicate the critical curves for slow (*dotted lines*), Alfvén (*solid lines*), and fast (*dashed lines*) speeds in the wind acceleration. The grayscale contours indicate the absolute value of the toroidal field component $|B_\phi|$. Starting from the reference solution in (A), we double the extent of the dead zone in (B), raise the field strength to twice its value in (C), and double both the dead zone extent and the field strength in (D).

quantitative agreement with the observations at these distances must await models in which we take the energy equation into account and/or model extra momentum addition as in Wang et al. (1998). The equatorial toroidal velocity profile is shown in Figure 4 (*right*). Note that increasing B_0 or enlarging the dead zone both negatively affect the degree to which the corona corotates with the star.

Keppens & Goedbloed (1999a) also contained a hydrodynamic solution for a much faster rotation rate quantified

by $\zeta = 0.3$, or 20 times the solar rotation rate. The additional centrifugal acceleration moves the sonic transition closer to the star along the equator and induces an equatorward streamline bending at the base at higher latitudes (see also Tsinganos & Sauty 1992). One could meaningfully ask what remains of this effect when a two-component field structure is present as well. Therefore, we calculate an MHD wind for this rotation rate, with $B_0 = 3.69$ and $\theta_{\text{wind}} = 60^\circ$ as in the reference case. The corresponding

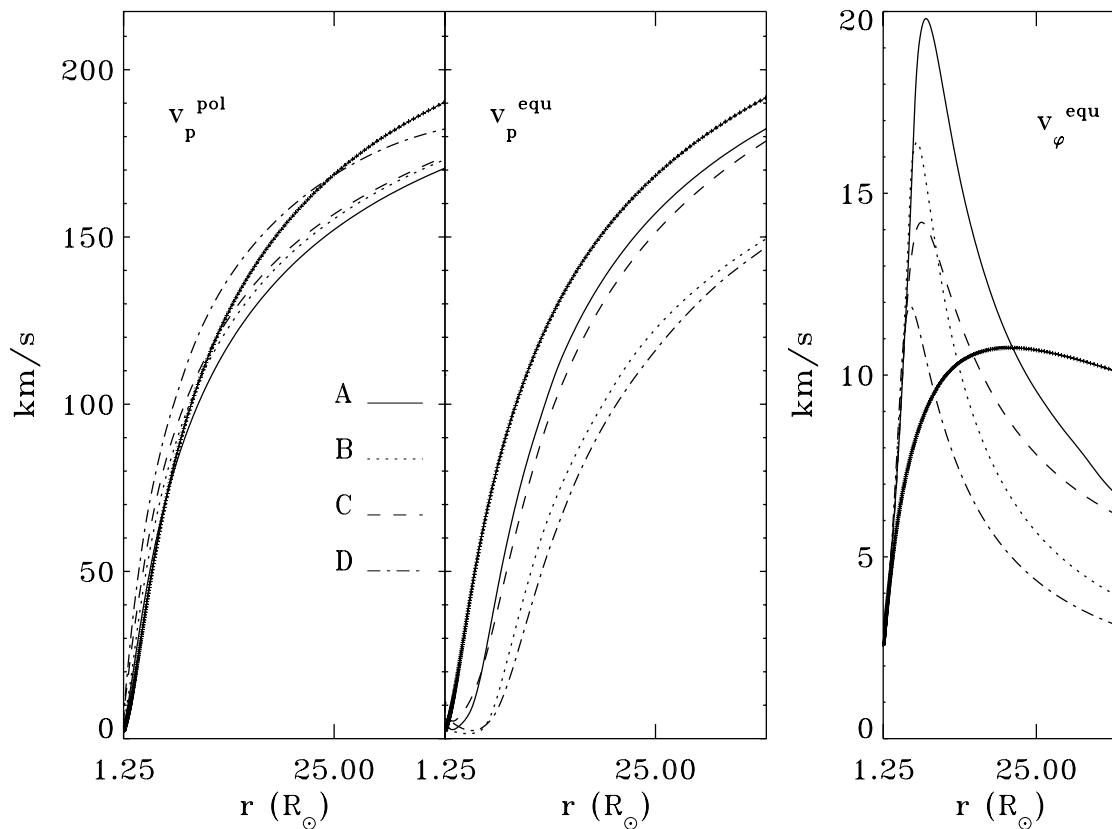


FIG. 4.—Comparison for the four solutions shown in Fig. 3. *Left*: Poloidal velocity at the pole as a function of radius. *Middle*: Poloidal velocity along the equator. *Right*: Toroidal velocity along the equator. In all three panels, the crosses indicate the same quantity for a solution with a split-monopole base field.

mass-loss rate parameter (only used in the wind zone) is $f_{\text{mass}} = 0.01553$. Figure 5 displays the wind structure as in Figure 3, with the grayscale indicating the logarithm of the density pattern. For this solution, we used the up-down symmetry to double the resolution in polar angle at the same computational cost. The shape of the critical curves has changed dramatically, with a significant outward poleward shift of the Alfvén curve and a clear separation between Alfvén and fast critical curves—in agreement with a 1.5D Weber-Davis prediction. The actual position of the critical surfaces may be influenced by an interaction with the outer boundary at $50r_*$ in the time stepping toward a stationary solution. In fact, the combined Alfvén-fast polar transition has shifted outside the computational domain, and the residual could not be decreased to arbitrary small values but stagnated at $\mathcal{O}(10^{-7})$ following this interaction. Within the plotted region of $\sim 37 R_\odot$, the solution is acceptable as explained in § 2. Note how the density structure shows an increase toward the equator, causing a very effective thermocentrifugal acceleration of the equatorial wind above the dead zone. The equatorward streamline bending occurring in the purely hydrodynamic wind is still important but is now clearly affected by the presence of the dead zone. The toroidal magnetic pressure built up by the stellar rotation along the midlatitude open field lines is shaping the wind structure as a whole. In those regions, we have $\rho v_p^2/B_\phi^2 < 1$ together with $2p/B_\phi^2 < 1$. Thereby, it also leads to streamline bending, both poleward as clearly seen in the high-latitude field lines and equatorward in the vicinity of the stellar surface. In this way, the magnetic topology consisting of a dead and a wind zone, combined with fast

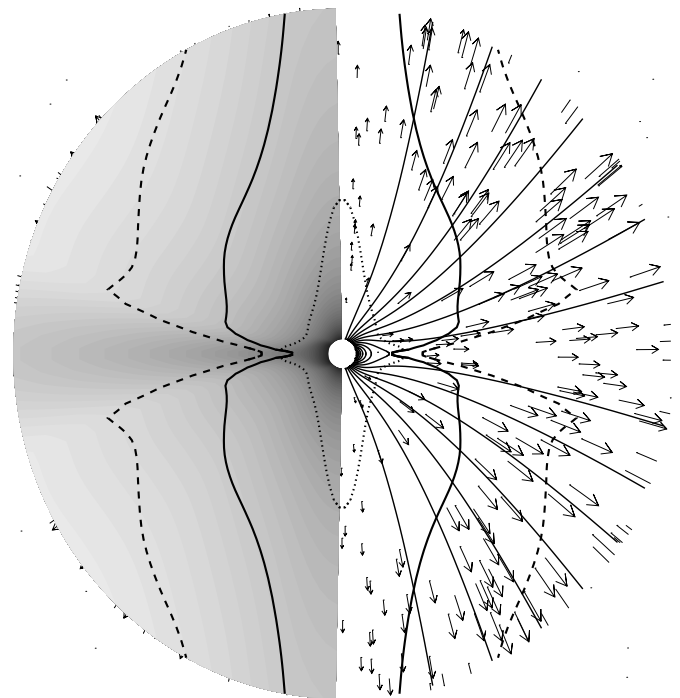


FIG. 5.—Magnetized wind solution for a star rotating 20 times faster than our reference “solar” solution. With the star at center, field lines and poloidal flow vectors are shown at right; density contours are given at left; and the critical slow (*dotted lines*), Alfvén (*solid lines*), and fast (*dashed lines*) curves are shown throughout the poloidal cut, stretching out to $37 R_\odot$.

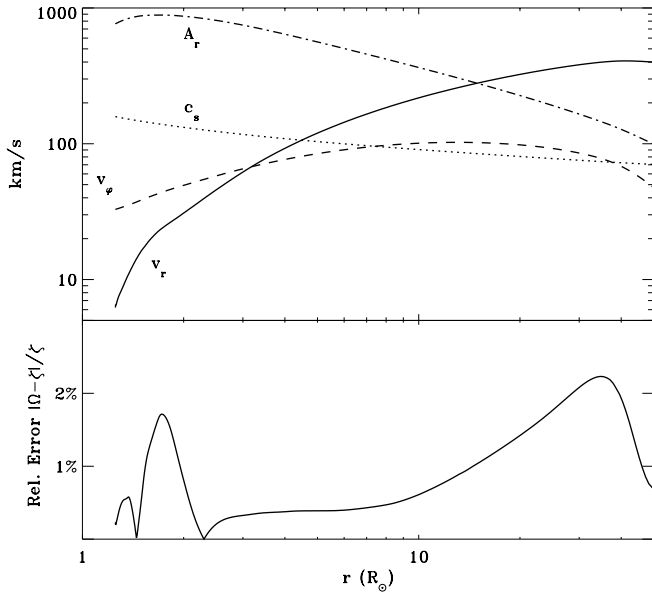


FIG. 6.—Purely radial cut through the wind solution from Fig. 5 at a polar angle of $\theta = 41.6^\circ$. The top panel shows the radial Alfvén speed A_r , sound speed c_s , radial velocity v_r , and azimuthal velocity v_ϕ . The bottom panel confirms the strict corotation achieved: the (flux) function Ω deviates less than 3% from its fixed base value ζ .

rotation, leads to magnetically dominated collimation along the stellar poles, together with magnetorotational deflections along the equator. The latter leads to enhanced densities in the equatorial plane.

Figure 6 shows the radial dependence at a polar angle $\theta = 41.6^\circ$ of the radial velocity v_r , sound speed c_s , radial Alfvén speed $A_r = B_r/\rho^{1/2}$, and azimuthal speed v_ϕ . Note that the radial velocity reaches up to 400 km s^{-1} (compare with the $\sim 200 \text{ km s}^{-1}$ velocities reached under solar conditions as shown in Fig. 4) as a result of the additional centrifugal acceleration. The rotation plays a significant dynamical role here, in contrast to the “solar-like” models discussed earlier and displayed in Figure 3. The toroidal speed v_ϕ reaches above 100 km s^{-1} , a factor of 10 higher than along the ecliptic as shown in Figure 4 (left). The corotation obtained by the numerical procedure to find the stationary state can again be quantified by the relative error $|\Omega - \zeta|/\zeta$: the bottom panel of Figure 6 proves that it is less than 3% along that same radial cut.

4. TRIGGERING CORONAL MASS EJECTIONS

In the process of generating a stationary wind solution, various dynamic phenomena take place which may have physical relevance. For instance, the equatorial conic section delineated by $\theta \in [\theta_{\text{wind}}, \pi - \theta_{\text{wind}}]$, which was initially static ($v_p = 0$) and dipolar throughout, first gets “invaded” by plasma emanating from the wind zone. The open field structure is dragged in toward the equator, and most of the dipolar field is moved out of the domain, except for the remaining “dead” zone. One could qualitatively relate some of these changes in the global magnetic topology with observed coronal phenomena.

In reality, however, coronal mass ejections represent major disturbances which happen on top of the stationary transonic solar wind. They are associated with sudden, significant mass loss and cause violent disruptions of the global field pattern. Most notably, one frequently observes

the global coronal wind structure to return to its previous stationary state, after the passage of the CME. Within the realms of our stellar wind models, we can trigger CMEs on top of the outflow pattern, study their motion, and at the same time demonstrate that the numerical solutions indeed are stable to such violent perturbations by returning to a largely unchanged stationary state. We still restrict ourselves to axisymmetric calculations, so the geometry of our “CME” events is rather artificial. In future work, we intend to model these CMEs in their true 3D setting.

As background stellar wind, we use a slightly modified model B from the previous section. Model B had a large dead zone, $\theta_{\text{wind}} = 30^\circ$, $B_0 = 3.69$, and a rigid rotation with $\zeta = 0.0156$ corresponding to $\Omega_\odot \sim 3 \times 10^{-6} \text{ s}^{-1}$. We changed the boundary condition on v_ϕ to mimic a “solar-like” differential rotation, by taking

$$\zeta(\theta) = \zeta_0 + \zeta_2 \cos^2 \theta + \zeta_4 \cos^4 \theta, \quad (15)$$

with $\zeta_0 = 0.0156$, $\zeta_2 = -0.00197$, and $\zeta_4 = -0.00248$. This forces the equator to rotate faster than the poles in accord with the observations. As expected for this low rotation rate, this has no significant influence on the wind acceleration pattern. The coronal mass ejection is an equally straightforward modification of the boundary condition imposed on the poloidal momentum equation, namely $\rho v_p = f_{\text{mass}}(\theta, t) \hat{e}_r/r^2$, with

$$f_{\text{mass}}(\theta, t) = f_{\text{wind}}(\theta) + g_{\text{CME}} \sin\left(\frac{\pi t}{\tau_{\text{CME}}}\right) \cos^2\left(\frac{\pi \theta - \theta_{\text{CME}}}{2 a_{\text{CME}}}\right), \quad (16)$$

for $0 \leq t \leq \tau_{\text{CME}}$ and $\theta_{\text{CME}} - a_{\text{CME}} \leq \theta \leq \theta_{\text{CME}} + a_{\text{CME}}$, and otherwise

$$f_{\text{mass}}(\theta, t) = f_{\text{wind}}(\theta). \quad (17)$$

The wind-related mass-loss rate $f_{\text{wind}}(\theta)$ contains the polar angle dependence due to the dead zone, as before. The extra four parameters control the magnitude of the CME mass-loss rate g_{CME} , the duration τ_{CME} , and the location θ_{CME} and extent $0 \leq a_{\text{CME}} \leq \pi/2$ in polar angle for the mass ejection. We only present one CME scenario for parameter values $g_{\text{CME}} = 2$, $\tau_{\text{CME}} = 0.5$, $\theta_{\text{CME}} = 60^\circ$, and $a_{\text{CME}} = 30^\circ$. Note that the up-down symmetry is hereby deliberately broken. This scenario mimics a mass ejection which detaches from the coronal base within 45 minutes and which has an associated mass flux of about $2 \times 10^{13} \text{ g s}^{-1}$. In fact, the total amount of mass lost due to the CME can be evaluated from

$$M_{\text{lost}}^{\text{CME}} = 2g_{\text{CME}} \tau_{\text{CME}} \frac{\pi^2}{\pi^2 - a_{\text{CME}}^2} [\cos(\theta_{\text{CME}} - a_{\text{CME}}) - \cos(\theta_{\text{CME}} + a_{\text{CME}})]. \quad (18)$$

For the chosen parameter values, this works out to be $M_{\text{lost}}^{\text{CME}} = (36/35)3^{1/2}$, corresponding to $0.98 \times 10^{17} \text{ g}$, a typical value for a violent event.

Figure 7 shows the density difference between the evolving mass ejection and the background stellar wind (left panel), the magnetic field structure (middle panel), and the toroidal velocity component v_ϕ (right panel) at times $t = 1$ (1 hr 27 minutes after onset) and $t = 3$ (4 hr 20 minutes after onset). The region is plotted up to $15r_* \simeq 18.75 R_\odot$. Although the event is triggered in the upper quadrant dead zone only, its violent character also disturbs the overlying open field (or wind) zone. The added plasma, trapped in the

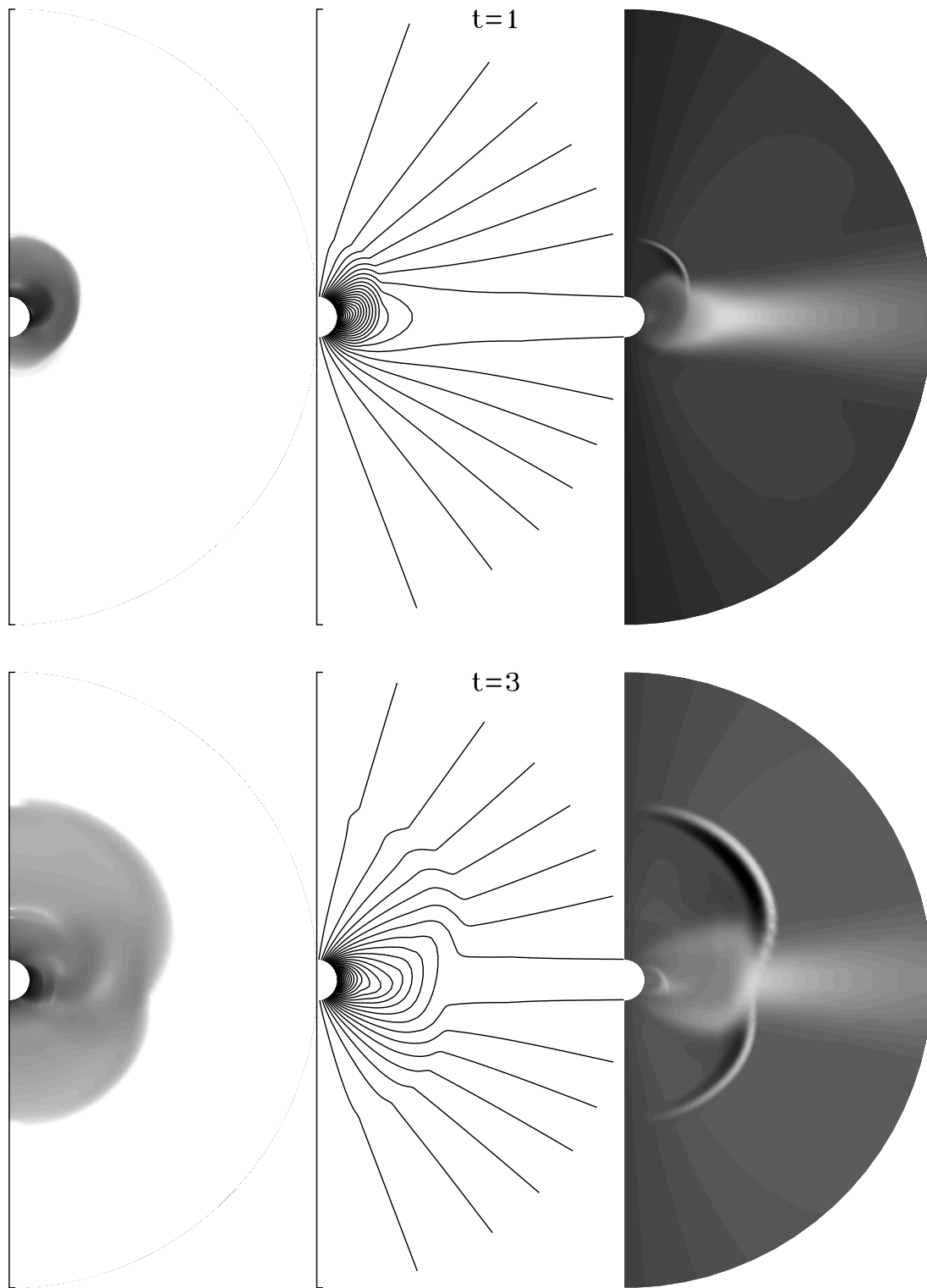


FIG. 7.—Coronal mass ejection simulated on top of an axisymmetric transonic wind. At the times indicated (1 hr 27 minutes and 4 hr 21 minutes after the onset), we show poloidal cuts. *Left*: Difference in the density pattern between the evolving CME and the original stationary wind solution. *Middle*: Poloidal field structure. *Right*: Toroidal velocity component.

dead zone, even perturbs the lower quadrant wind zone at later times. Note that the CME induces global, abrupt changes in the toroidal velocity component. The outermost closed field lines get stretched out radially, pulling the dead zone along (see Figs. 7–8). In ideal MHD calculations, they can never detach through reconnection, although numerical

diffusion can cause it to happen. We observed the outermost field lines of the dead zone to travel outward without noticeable reconnection. The overall wind pattern in the first 15 base radii thereby approximately returns to its original stationary state, as shown in Figure 8 which gives the solution at $t = 5$ (7 hr 13 minutes after onset) and $t = 30$

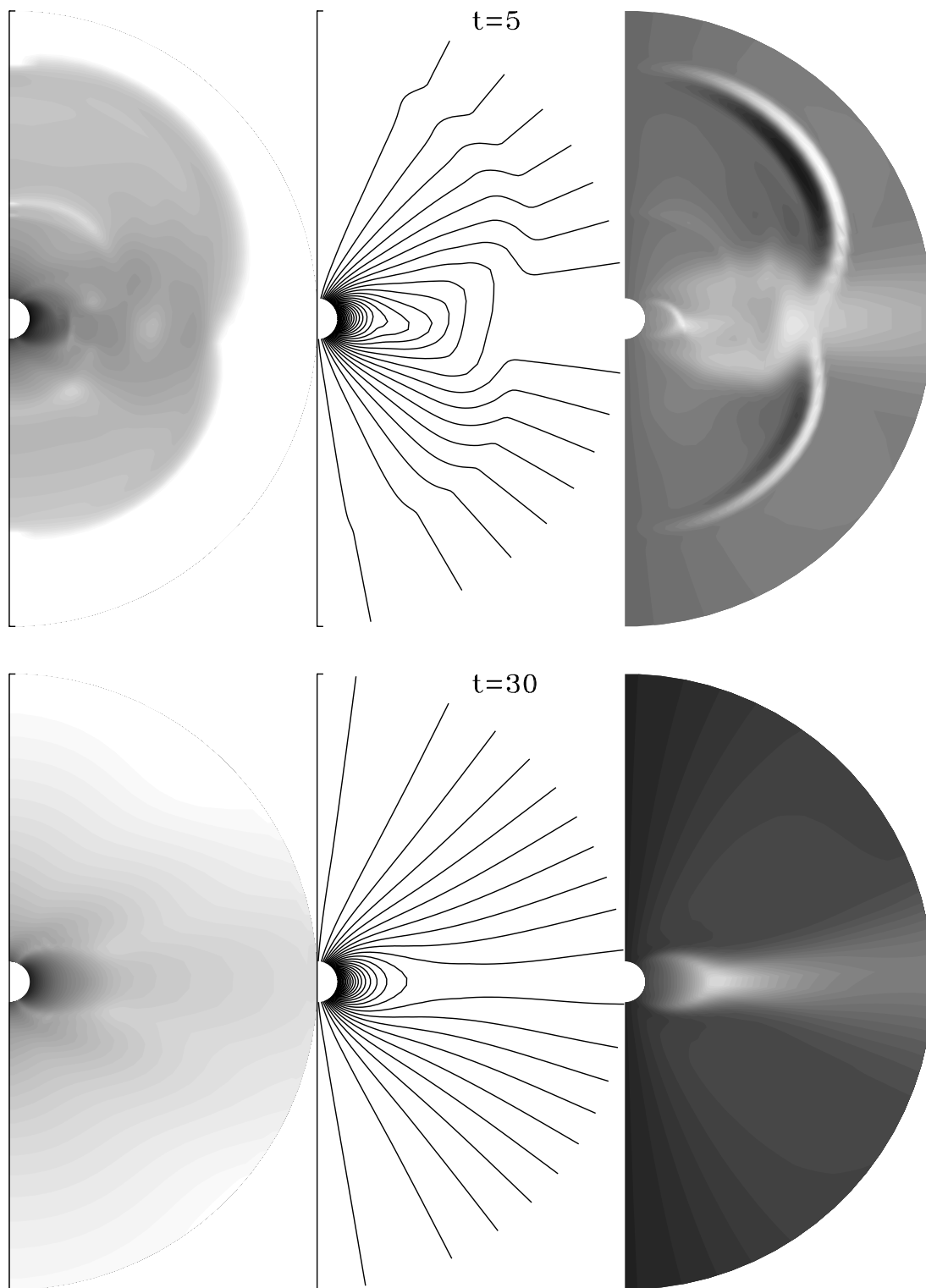


FIG. 8.—As Fig. 7, times corresponding to 7 hr 13 minutes and 43 hr past the onset. Note how the solution returns to a state almost identical to the original stationary wind solution.

(more than 43 hr after onset). Figure 9 shows how a hypothetical spacecraft at $21r_* \sim 26.23 R_\odot$, close to the ecliptic, would record the CME passage as a sudden increase in density and poloidal velocity which eventually relax to their pre-event levels. The event is followed by an increased azimuthal flow regime and shows large-amplitude oscillations in magnetic field strength and orientation.

As we assumed axisymmetry, this simulation serves as a crude model for CME-type phenomena. Interestingly, axisymmetric numerical simulations of toroidal flux “belts” launched from within the dead zone of a purely meridional, polytropic MHD wind can relate favorably to satellite magnetic cloud measurements at 1 AU (Wu et al. 1999). Note that we triggered a “CME” by prescribing a time- and

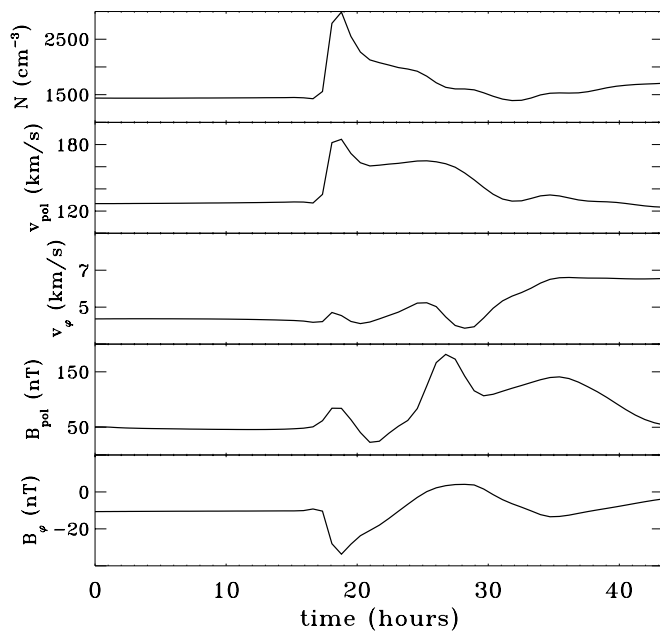


FIG. 9.—In situ measurement of a CME passage: number density, poloidal velocity, toroidal velocity, poloidal field strength, and toroidal field as a function of time at a fixed position of $26.23 R_{\odot}$ and an angle of $2^{\circ}25'$ above the ecliptic.

space-dependent mass flux at the stellar base, where the density and the magnetic field components could adjust freely. Alternatively, as used in studies by Mikić & Linker (1994), global coronal restructuring can be triggered by shearing a coronal arcade. Parameter studies of axisymmetric, but ultimately 3D solutions, could investigate the formation and appearance of various MHD shock fronts depending on plasma beta, Mach numbers, etc.

5. CONCLUSIONS AND OUTLOOK

Continuing our gradual approach toward dynamic stellar wind simulations in three dimensions, we studied the influence of (1) the magnetic field strength and topology (allowing for wind and dead zones), (2) the stellar rotation, and (3) sudden mass ejection on axisymmetric MHD winds.

We demonstrated how reasonable changes in the coronal magnetic field (factor of 2 in field strength and in dead zone extent) influence the detailed acceleration behavior of the wind. Larger dead zones cause effective, fairly isotropic acceleration to super-Alfvénic velocities since the polar, open field lines are forced to fan out rapidly with radial distance. The Alfvén transition moves outward when the coronal field strength increases. The equatorial wind outflow is in these models sensitive to the presence and extent of the dead zone, but has, by construction, a vanishing B_{ϕ} and a $\beta > 1$ zone from the tip of the dead zone to large radial distances. The parameter values for these models are solar-like, hence the winds are mostly thermally driven and, in particular, emanated from slowly rotating stars.

For a rotation rate, 20 times faster than solar, the wind structure changes dramatically, with a clear separation of the Alfvén and fast magnetosonic critical curves. At these rotation rates, a pure hydrodynamic model predicts equatorward streamline bending from higher latitudes. Our MHD models show how this is now mediated by the dipolar dead zone. An equatorial belt of enhanced density

stretches from above the dead zone outward, where effective thermocentrally driven outflow occurs. The magnetic field structure shows signs of a strong poleward collimation, due to the significant toroidal field pressure buildup at these spin rates. As pointed out by Tsinganos & Bogovalov (1999), this situation could apply to our own Sun in an earlier evolutionary phase.

It could be of interest to make more quantitative parameter studies of the interplay between field topology, rotation rate, etc., in order to apprehend transonic stellar outflows driven by combinations of thermal, magnetic, and centrifugal forces. A systematic study of the angular momentum loss rates as a function of dead zone extent, magnetic field strength, and rotation rate can aid in stellar rotational evolution modeling (Keppens, MacGregor, & Charbonneau 1995; Keppens 1997). Specifically, Li (1999) pointed out that the present solar magnetic breaking rate is consistent with either one of two magnetic topologies: (1) one with the standard coronal field strength of ~ 1 G and a small (less than $2 R_{\odot}$) dead zone or (2) one with a larger ~ 5 G dipole strength and a sizeable dead zone. When we calculate the torque exerted on the star by the magnetized winds A, B, C, and D shown in Figure 3 as

$$\tau_{\text{wind}} = 4\pi \int_0^{\pi/2} d\theta \Lambda \rho r^2 v_R \quad (19)$$

(noting the axi- and up-down symmetry), we find $\tau_{\text{wind}}^A \simeq 0.139 \times 10^{31}$ dyn cm, $\tau_{\text{wind}}^B \simeq 0.062 \times 10^{31}$ dyn cm, $\tau_{\text{wind}}^C \simeq 0.246 \times 10^{31}$ dyn cm, and $\tau_{\text{wind}}^D \simeq 0.123 \times 10^{31}$ dyn cm. This confirms Li's result, since a simultaneous doubling of the coronal field strength and the dead zone extent (from model A to D) hardly changes the torque magnitude. As could be expected, enlarging only the dead zone lowers the breaking efficiency (as pointed out in Solanki, Motamen, & Keppens 1997), while raising only the field strength leads to faster spin-down. Interestingly, a Weber-Davis prediction with governing parameters identical to the reference model A (as presented in Keppens & Goedbloed 1999a) gives a value $\tau_{\text{wind}} = 4\pi \rho_A r_A^2 v_{rA} \frac{2}{3} \Omega_* r_A^2 \simeq 2.387 \times 10^{31}$ dyn cm (all quantities evaluated at the Alfvén radius r_A), 1 order of magnitude larger! The same conclusion was reached by Priest & Pneuman (1974) by estimating the angular momentum loss rate from the purely meridional Pneuman & Kopp (1971) model. Although the latter model does not include rotation (so that Λ in eq. [19] is strictly zero for this model), Priest & Pneuman (1974) could estimate the torque for a solar rotation rate from the obtained variation of the poloidal Alfvén radius as a function of latitude (Fig. 2, right panel). The resulting estimate was only 15% of that for a monopole base field. Our exactly evaluated spin-down rates are 2.6%–10.3% of a split-monopole case. The large difference arises due to the presence of the dead zone and the fact that B_{ϕ} vanishes across the equator for the wind solutions from Figure 3. Indeed, evaluating the torque from equation (19) for the monopolar wind solution from Keppens & Goedbloed (1999a; their Fig. 4) gives $\tau_{\text{wind}} \simeq 2.326 \times 10^{31}$ dyn cm, in agreement with the Weber-Davis estimate. Hence, it should be clear that full MHD modeling is a useful tool to further evaluate and constrain different magnetic breaking mechanisms.

We showed how CME events can be simulated on top of these transonic outflows. The detailed wind structure is stable to violent mass dumps, even when ejected in the dead zone. Note that we restricted ourselves to axisymmetric per-

turbations, and it will be of interest to show whether the axisymmetric solutions are similarly stable to non-axisymmetric perturbations (as recently investigated for shocked accretion flows on compact objects in Molteni, Tóth, & Kuznetsov 1999). One could then focus on truly 3D mass ejecta and their parametric dependence (possibly allow for direct comparison with Large-Angle Spectrometric Coronagraph observations of coronal mass ejections), or even experiment with unaligned rotation and magnetic axes. A 3D time-dependent analytic model by Gibson & Low (1998) can be used as a further check on the numerics. Alternatively, we may decide to zoom in on (3D) details of the wind structure at the boundaries of open and closed field-line regions or about the ecliptic plane, to see

whether shear flow-driven Kelvin-Helmholtz instabilities (Keppens et al. 1999b; Keppens & Tóth 1999b) develop in these regions.

The Versatile Advection Code was developed as part of the project on Parallel Computational Magneto-Fluid Dynamics, funded by the Dutch Science Foundation (NWO) Priority Program on Massively Parallel Computing and coordinated by J. P. G. Computer time on the Cray C90 was sponsored by the Dutch Stichting Nationale Computerfaciliteiten (NCF). We thank Keith MacGregor for suggesting to compare torque magnitudes for different models and an anonymous referee for making several useful comments.

REFERENCES

- Brackbill, J. U., & Barnes, D. C. 1980, *J. Comput. Phys.*, 35, 426
 Collela, P., & Woodward, P. R. 1984, *J. Comput. Phys.*, 54, 174
 Gallagher, P. T., Mathioudakis, M., Keenan, F. P., Phillips, K. J. H., & Tsinganos, K. 1999, *ApJ*, 524, L133
 Gibson, S. E., & Low, B. C. 1998, *ApJ*, 493, 460
 Goedbloed, J. P., Keppens, R., & Lifschitz, A. 1998, in *Proc. 25th EPS Conference on Controlled Fusion and Plasma Physics*, ed. P. Pavlo (Europhysics Conference Abstracts Volume 22C; European Physical Society; CD-ROM), 1118
 Goedbloed, J. P., & Lifschitz, A. 1997, *Phys. Plasmas*, 4(10), 3544
 Grall, R. R., Coles, W. A., KlingleSmith, M. T., Breen, A. R., Williams, P. J. S., Markkanen, J., & Esser, R. 1996, *Nature*, 379, 429
 Hassler, D. M., Dammasch, I. E., Lemaire, P., Brekke, P., Curdt, W., Mason, H. E., Vial, J.-C., & Wilhelm, K. 1999, *Science*, 283, 810
 Holzer, T. E., & Leer, E. 1997, in *Proc. Fifth SOHO Workshop on the Corona and Solar Wind near Minimum Activity*, ed. A. Wilson (ESA SP-404; Noordwijk: ESA), 65
 Keppens, R. 1997, *A&A*, 318, 275
 Keppens, R., & Goedbloed, J. P. 1999a, *A&A*, 343, 251
 Keppens, R., & Goedbloed, J. P. 1999b, in *Proc. SOHO-7 Workshop*, *Space Sci. Rev.*, 87, 223
 Keppens, R., MacGregor, K. B., & Charbonneau, P. 1995, *A&A*, 294, 469
 Keppens, R., & Tóth, G. 1999a, in *Vector and Parallel Processing—VECPAR '98*, ed. J. M. L. M. Palma, J. Dongarra, & V. Hernandez (Lecture Notes in Computer Science 1573; Berlin: Springer), 680
 Keppens, R., & Tóth, G. 1999b, *Phys. Plasmas*, 6(5), 1461
 Keppens, R., Tóth, G., Botchev, M. A., & van der Ploeg, A. 1999a, *Int. J. Numer. Methods Fluids*, 30, 335
 Keppens, R., Tóth, G., Westermann, R. H. J., & Goedbloed, J. P. 1999b, *J. Plasma Phys.*, 61(1), 1
 Li, J. 1999, *MNRAS*, 302, 203
 Lifschitz, A., & Goedbloed, J. P. 1997, *J. Plasma Phys.*, 58, 61
 McComas, D. J., et al. 1998, *Geophys. Res. Lett.*, 25(1), 1
 Mikić, Z., & Linker, J. A. 1994, *ApJ*, 430, 898
 Molteni, D., Tóth, G., & Kuznetsov, O. A. 1999, *ApJ*, 516, 411
 Nerney, S. F., & Suess, S. T. 1975, *ApJ*, 196, 837
 Parker, E. N. 1958, *ApJ*, 128, 664
 Pneuman, G. W., & Kopp, R. A. 1971, *Sol. Phys.*, 18, 258
 Priest, E. R., & Pneuman, G. W. 1974, *Sol. Phys.*, 34, 231
 Sakurai, T. 1985, *A&A*, 152, 121
 Sakurai, T. 1990, *Comput. Phys. Rep.*, 12, 247
 Solanki, S. K., Motamen, S., & Keppens, R. 1997, *A&A*, 324, 943
 Suess, S. T., & Nerney, S. F. 1973, *ApJ*, 184, 17
 Tóth, G. 1996, *Astrophys. Lett. Commun.*, 34, 245
 Tóth, G. 1997, in *Proc. High Performance Computing and Networking Europe 1997*, ed. B. Hertzberger B. & P. Sloot (Lecture Notes in Computer Science 1225; Berlin: Springer), 253
 Tóth, G., & Keppens, R. 1998, in *Proc. High Performance Computing and Networking Europe 1998*, ed. P. Sloot, M. Bubak, & B. Hertzberger (Lecture Notes in Computer Science 1401; Berlin: Springer), 368
 Tóth, G., Keppens, R., & Botchev, M. A. 1998, *A&A*, 332, 1159
 Tóth, G., & Odstrčil, D. 1996, *J. Comput. Phys.*, 128, 82
 Totten, T. L., Freeman, J. W., & Arya, S. 1995, *J. Geophys. Res.*, 100, 13
 Trussoni, E., Tsinganos, K., & Sauty, C. 1997, *A&A*, 325, 1099
 Tsinganos, K., & Bogovalov, S. 1999, *A&A*, submitted
 Tsinganos, K., & Sauty, C. 1992, *A&A*, 255, 405
 Ustyugova, G. V., Koldoba, A. V., Romanova, M. M., Chechetkin, V. M., & Lovelace, R. V. E. 1999, *ApJ*, 516, 221
 van der Ploeg, A., Keppens, R., & Tóth, G. 1997, in *Proc. High Performance Computing and Networking Europe 1997*, ed. B. Hertzberger & P. Sloot (Lecture Notes in Computer Science 1225; Berlin: Springer), 421
 Wang, A. H., Wu, S. T., Suess, S. T., & Poletto, G. 1998, *J. Geophys. Res.*, 103(A2), 1913
 Weber, E. J., & Davis, L. 1967, *ApJ*, 148, 217
 Wu, S. T., Guo, W. P., & Dryer, M. 1997, *Sol. Phys.*, 170, 265
 Wu, S. T., Guo, W. P., Michels, D. J., & Burgala, L. F. 1999, *J. Geophys. Res.*, 104(A7), 14789